JACS
JOURNAL OF THE AMERICAN CHEMICAL SOCIETY
Article
pubs.acs.org/JACS

# Vacancy-Induced Ferromagnetism of $MoS_2$ Nanosheets

Liang Cai,[†,§] Jingfu He,[†,§] Qinghua Liu,[†] Tao Yao,[†] Lin Chen,[†] Wensheng Yan,*[,†] Fengchun Hu,[†] Yong Jiang,[†] Yidong Zhao,[‡] Tiandou Hu,[‡] Zhihu Sun,*[,†] and Shiqiang Wei*[,†]

[†]National Synchrotron Radiation Laboratory, University of Science and Technology of China, Hefei 230029, P. R. China
[‡]Beijing Synchrotron Radiation Facility, Institute of High Energy Physics, Chinese Academy of Sciences, Beijing 100049, P. R. China

Supporting Information

**ABSTRACT:** Outstanding magnetic properties are highly desired for two-dimensional ultrathin semiconductor nanosheets. Here, we propose a phase incorporation strategy to induce robust room-temperature ferromagnetism in a nonmagnetic $MoS_2$ semiconductor. A two-step hydrothermal method was used to intentionally introduce sulfur vacancies in a 2H-$MoS_2$ ultrathin nanosheet host, which prompts the transformation of the surrounding 2H-$MoS_2$ local lattice into a trigonal (1T-$MoS_2$) phase. 25% 1T-$MoS_2$ phase incorporation in 2H-$MoS_2$ nanosheets can enhance the electron carrier concentration by an order, introduce a $Mo^{4+}$ 4d energy state within the bandgap, and create a robust intrinsic ferromagnetic response of 0.25 $\mu_B$/Mo by the exchange interactions between sulfur vacancy and the $Mo^{4+}$ 4d bandgap state at room temperature. This design opens up new possibility for effective manipulation of exchange interactions in two-dimensional nanostructures.

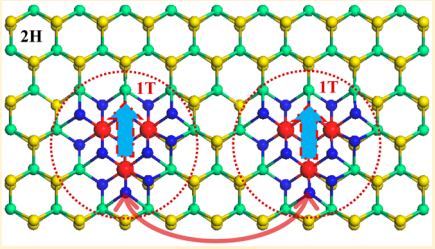


## INTRODUCTION

Over the past a few years, two-dimensional (2D) nanosheets, exemplified by the well-known graphene, have been widely studied due to their unique mechanical and electronic properties that render them with numerous potential applications.[1−4] Among them, $MoS_2$ nanosheets have attracted special attention because they possess outstanding electronic features of high charge-carrier mobility, tunable charge-carrier types, and high on/off ratio.[5,6] $MoS_2$ nanosheets-based semiconductor devices, such as field-effect transistors[7,8] and digital circuits,[9] have been successfully fabricated. Besides, $MoS_2$ materials have especially well-defined spin-splitting property that is very suitable for spintronics applications.[5,10] Unfortunately, the nonmagnetic property of common $MoS_2$ nanosheets has hampered its applications in spintronics. If the nonmagnetic $MoS_2$ nanosheets could be endowed with robust room-temperature ferromagnetism, they could be expected to not only act as an ideal spintronics channel material for nanodevices but also provide an excellent platform for studying the relationship between electronic and magnetic properties of quantum-confined matters.[2,11] How to realize and manipulate ferromagnetic property in $MoS_2$ nanosheets then becomes a critical issue to be resolved.

To obtain ferromagnetic $MoS_2$ nanosheets and other low-dimensional materials, traditional methods, such as doping of foreign magnetic ions or annealing under different atmospheres,[12] have been attempted but met with limited success.[13−15] Recently, other ways of introducing ferromagnetism into $MoS_2$ nanosheets have been explored from both theoretical and experimental aspects.[16−21] First-principles calculations by Zheng et al. predicted that macroscopic ferromagnetism of $MoS_2$ nanosheets could be introduced by applying equibiaxial strain and doping vacancy.[16] Zhang et al. used vertically aligned edge-oriented $MoS_2$ nanosheets to form ferromagnetic $MoS_2$ films, the thickness of which is changed to afford Mo and S ions with unsaturated bonds.[20] However, the as-activated ferromagnetism of $MoS_2$ nanosheets is unstable and can be easily removed by local structural rearrangements during annealing or chemical passivation processes.[22] More approaches are still desired to introduce robust ferromagnetic interactions in freely expanded $MoS_2$ nanosheets. This could be inspired by the fact that $MoS_2$ has various atomic arrangements and electronic structures, which provides a solid foundation for manipulating the electronic properties of Mo ions via tailoring the atomic structures.[23] For instance, the trigonal prismatic $MoS_2$ (2H-$MoS_2$) phase is able to transform to octahedral (1T) phase by electron doping (electron irradiation or introducing Li ions).[24,25] Among numerous $MoS_2$ phases, 2H-$MoS_2$ is macroscopically nonmagnetic, because the $Mo^{4+}$ ions are in a trigonal prismatic local coordination in which the two 4d electrons are spin-antiparallel and the net magnetic moment is zero. If the $Mo^{4+}$ 4d electron configuration could be tuned to have nonzero magnetic moment, the 2H-$MoS_2$ phase could also display magnetic properties. An effective method following this line is incorporating another phase of $MoS_2$ into the 2H-$MoS_2$ matrix, a concept called "phase incorporation" (Figure 1a). The 1T-$MoS_2$ phase is a good candidate to be incorporated, because it has a magnetic moment of 2 $\mu_B$/Mo ions and its crystal structure is very similar to that of 2H-$MoS_2$.[26] More importantly, the Mo atoms in 1T-$MoS_2$ have identical atomic positions as in 2H-$MoS_2$; therefore, the incorporated 1T-$MoS_2$

Received: November 26, 2014
Published: January 30, 2015




DOI: 10.1021/ja5120908
J. Am. Chem. Soc. 2015, 137, 2622−2627

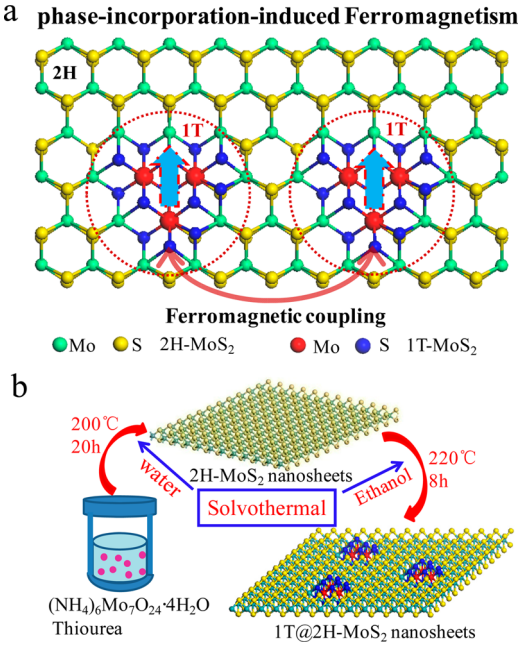


**Figure 1.** (a) Diagrammatic representation of the phase incorporation strategy to achieve ferromagnetism of 2H-$MoS_2$ nanosheets. (b) Schematic representation of the two-step hydrothermal synthetic route for the 1T@2H-$MoS_2$ nanosheets.

does not change the distributions of Mo ions in the 2H-$MoS_2$ (Figure 1a) and does not hamper its practical applications. Motivated by the above consideration, we anticipate that introducing the 1T phase of $MoS_2$ into the 2H-$MoS_2$ nanosheets could be an effective strategy for combining the semiconductor character of 2H-$MoS_2$ with the magnetic feature of 1T-$MoS_2$.

In this work, the phase-incorporation strategy is employed to induce ferromagnetism into the originally nonmagnetic 2D nanosheet materials. Taking 2H-$MoS_2$ nanosheets as a prototype material and using a two-step hydrothermal synthesis method (Figure 1b), we successfully incorporated 1T-$MoS_2$ phase into the matrix of 2H-$MoS_2$ nanosheet and observed its robust ferromagnetic response with a magnetic moment of 0.25 $\mu_B$/Mo at room temperature. It is further revealed that the interaction between the Mo 4d states of the 1T-$MoS_2$ dopant and a bandgap energy state induced by sulfur vacancy is the origin of the ferromagnetism of the phase-incorporated $MoS_2$ nanosheets. Our results provide a new hint for manipulating the ferromagnetic interaction in 2D semiconductors.

## RESULTS AND DISCUSSION

The 1T phase incorporated 2H-$MoS_2$ nanosheets (hereafter called 1T@2H-$MoS_2$ nanosheets) were obtained by a two-step hydrothermal synthetic strategy, as depicted schematically in Figure 1b. The critical step in the synthesis is the control over the formation of sulfur vacancy ($V_S$) in the 2H-$MoS_2$ nanosheets. The initial 2H-$MoS_2$ nanosheets were formed from autoclaving Mo ions precursor and thiourea at a high temperature of 200 °C. Then the $MoS_2$ nanosheets were subjected to centrifugation, ultrasonation in ethanol solution, and once more autoclavation at 220 °C for 8 h to facilitate the generation of $V_S$ and transform the local lattice of 2H-$MoS_2$ surrounding sulfur vacancies into 1T phase, finally resulting in the formation of 1T@2H-$MoS_2$ nanosheets. The role of $V_S$ is similar to that of a lithium ion occupying the interlayer S−S tetrahedron site in lithiated $MoS_2$ which undergoes a 2H-IT phase transition.[25]

To verify the success of the two-step hydrothermal synthesis strategy in obtaining the 1T@2H-$MoS_2$ nanosheets, detailed structure information on the as-synthesized product is unraveled by the atomic force microscopy (AFM), high-resolution transmission electron microscopy (HRTEM), and Raman spectra as shown in Figure 2a−c. The HRTEM images of the 1T@2H-$MoS_2$ nanosheets show distinct lattice fringes of 0.27 nm with 60° angles attributed to the (100) and (010) planes of 2H-$MoS_2$, respectively, suggesting the exposure of the

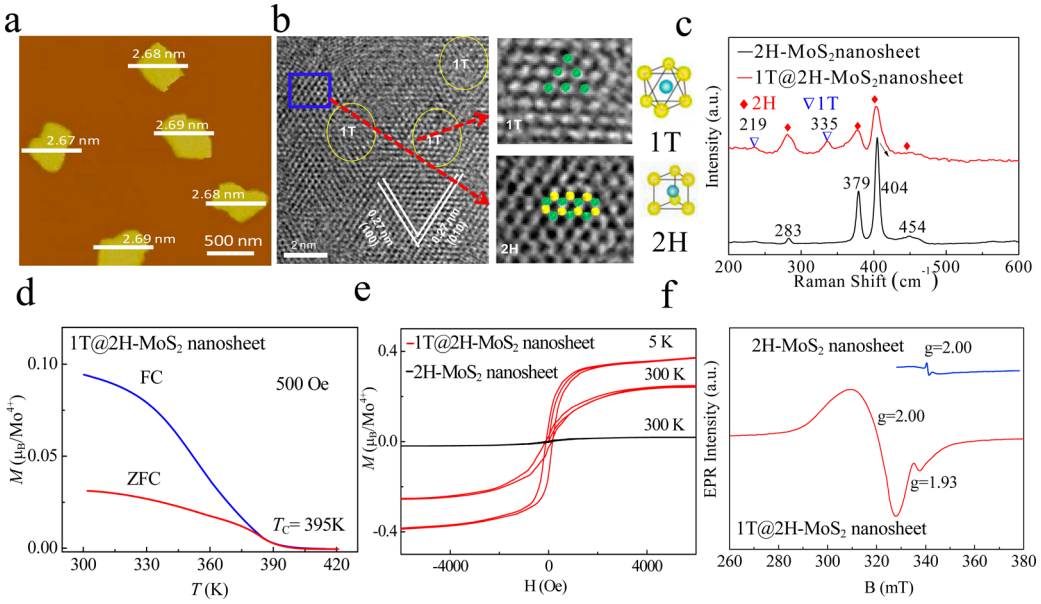


**Figure 2.** Characterization of the 1T@2H-$MoS_2$ nanosheets. (a) AFM image, (b) HRTEM image, (c) Raman spectrum, (d) temperature dependence of FC and ZFC magnetization ($M$−$T$ curves), (e) magnetization vs magnetic field ($M$−$H$) curves at 5 and 300 K, and (f) EPR spectrum. For comparison, in (c), (e), and (f), the corresponding data for 2H-$MoS_2$ nanosheets are also displayed.



DOI: 10.1021/ja5120908
J. Am. Chem. Soc. 2015, 137, 2622−2627

(001) facets of the 2H-$MoS_2$ matrix. This point is also supported by the XRD patterns (Figure S1). The lateral size of the 2D nanosheets is up to about 0.4 $\mu$m (Figures 2a and S2), and the statistical height profiles show a smooth morphology with a thickness of about 2.67 nm, very close to two $z$-axis unit-cell thicknesses of the 2H-$MoS_2$ phase. Moreover, from the HRTEM images, the implanted 1T-$MoS_2$ phase in the 2H-$MoS_2$ matrix could be clearly visualized as indicated by the circles in Figure 2b. The zoom-in HRTEM images (Figure 2b) evidently display some trigonal lattice area (octahedral coordination) of the 1T phase, besides the common honeycomb lattice area of the trigonal prismatic coordination in the 2H phase. Furthermore, for the 2H-$MoS_2$ nanosheets, the Raman spectra (Figure 2c) display characteristic peaks at 283, 379, 404, and 454 $cm^{-1}$ arising from the $E_{1g}$, $E^1_{2g}$, $A_{1g}$ and longitudinal acoustic phonon modes.[27,28] By contrast, for the 1T@2H-$MoS_2$ nanosheets, additional peaks at 219 and 335 $cm^{-1}$ attributed to the 1T-$MoS_2$ phase appear, suggesting the existence of a considerable amount of 1T phase ingredient embedded in the 2H-$MoS_2$ host.[29] All of these results lead us to believe that the 1T-$MoS_2$ is successfully implanted in the 2H-$MoS_2$ nanosheet matrix.

Next, for examining the magnetic properties of the as-synthesized 1T@2H-$MoS_2$ nanosheets, we measured the magnetization ($M-T$) curves against temperature under zero-field-cooling (ZFC) and field-cooling (FC) modes, as shown in Figure 2d. These measurements show that the 1T@2H-$MoS_2$ nanosheets have a Curie temperature of 395 K. We also measured the magnetizations curves ($M-H$) as a function of the applied magnetic field $H$ (Figure 2e) at 5 and 300 K for 1T@2H-$MoS_2$ nanosheets. For comparison, the $M-H$ curve of 2H-$MoS_2$ nanosheets at 300 K is also shown. The well-defined hysteresis loops indicate the room-temperature ferromagnetic behavior of both samples, different from the nonmagnetic property of bulk $MoS_2$. Figure S3 shows that the remanence and saturation magnetization of 2H-$MoS_2$ nanosheets are 0.002 $\mu_B$/Mo (0.1emu/g) and 0.02 $\mu_B$/Mo (1emu/g) at 300 K, respectively, close to the results reported by Zhang et al. on $MoS_2$ nanosheet films.[17] When part of the 2H phase is converted into 1T phase to form 1T@2H-$MoS_2$, the remanence and saturation magnetization are increased by 1 order, i.e., 0.02 and 0.25 $\mu_B$/Mo, respectively, demonstrating the significant impact of 1T-$MoS_2$ phase to the magnetic properties of 2H-$MoS_2$ nanosheets. When the temperature is decreased from 300 to 5 K, the saturation magnetization is increased from 0.25 to 0.35 $\mu_B$/Mo.

The high saturation magnetization (0.35 $\mu_B$/Mo at 5 K, 0.25 $\mu_B$/Mo at 300 K) of 1T@2H-$MoS_2$ nanosheets cannot come from either measurement artifacts or impurities. If we assume that the magnetism were originated from ferromagnetic impurities or contaminants (metallic Co clusters, for instance) that had been induced unintentionally during synthesis, from the measured saturation magnetization (0.35 $\mu_B$/atom at 5 K) and that (1.7 $\mu_B$/atom) of a Co ion in Co metal clusters, we could estimate the molar percentage of these Co clusters to be 10%. In fact, such a high level of Co clusters (and other magnetic impurities) was never observed in our XRD, XPS, energy dispersive spectroscopy (EDS) spectra and inductively coupled plasma (ICP) measurements (see Figure S4 and Table S1) within their detection limits. We also processed $Al_2O_3$ powders under the same treating conditions and using the same vessels as we did for 1T@2H-$MoS_2$ nanosheets, but never observed any trace of ferromagnetism. This also helps to exclude the possibility of introducing magnetic impurities during the synthesis of 1T@2H-$MoS_2$ nanosheets. Moreover, the Curie temperature ($T_C$ = 395 K) of our 1T@2H-$MoS_2$ nanosheets is quite different from that of $CoS_2$ ($T_C$ = 121 K) and $CoFeS_2$ ($T_C$ = 150 K) magnetic semiconductors.[17] All of these results lead us to conclude that the observed ferromagnetism of 1T@2H-$MoS_2$ is an intrinsic nature of this material.

To explore the source of magnetism of both $MoS_2$ nanosheets, we measured their EPR spectra as shown in Figure 2f. Both samples display a signal at $g$ = 2.00 that arises from sulfur vacancy ($V_S$); but the signal of 1T@2H-$MoS_2$ nanosheets is significantly intensified and broadened,[30] suggesting the increased concentration of $V_S$. More importantly, the 1T@2H-$MoS_2$ nanosheets also present a weak EPR signal at $g$ = 1.93 that implies the existence of a paramagnetic center. Considering the electronic features of the 1T- and 2H-$MoS_2$ phases, the paramagnetic center could only come from the unpaired Mo 4d electrons in 1T-$MoS_2$,[31] since all the electrons in 2H-$MoS_2$ are paired. Ochsenbein et al. observed in Mn-doped ZnO remarkably broadened paramagnetic signal of Mn ions upon introduction of alien electrons (acting as a new paramagnetic center) and hence concluded the interactions between Mn ions and alien electrons.[32] Similar phenomenon is also observed for our 2H-$MoS_2$ nanosheets upon incorporating part of 1T phase, implying the strengthen interactions between $V_S$ and $Mo^{4+}$ ions. Besides, the $V_S$–$Mo^{4+}$ interactions will also be inferred from the Mo $L_3$-edge XANES spectra (Figure S5). These experimental results lead us to speculate that the enhanced ferromagnetism in 1T@2H-$MoS_2$ nanosheets is intimately correlated with the strengthened $Mo^{4+}$–$V_S$ exchange interactions. The weak ferromagnetic response observed in the 2H-$MoS_2$ nanosheets is likely related to some complex consisting of S vacancy.[33]

In order to further verify the doping of 1T-$MoS_2$ phase and to determine its relative content in the 1T@2H-$MoS_2$ nanosheets, we employed the X-ray absorption fine structure (XAFS) and X-ray photoelectron spectroscopy (XPS) techniques to probe their local atomic structures. As shown in Figure 3a, the Mo K-edge X-ray absorption near-edge structure (XANES) spectrum of 2H-$MoS_2$ nanosheets exhibits four characteristic peaks A, B, C, and D. In contrast, the 1T@2H-$MoS_2$ nanosheets display quite different spectral features: peak D disappears, while a new peak $A_1$ emerges between peaks A and B. These distinct spectral features could be reproduced by XANES calculations using FEFF8.2 code for two structure models (see the details of structure model configurations and calculations in Section II in the Supporting Information). Model **A** refers to a 2H-$MoS_2$ cluster composed of 172 atoms, and model **B** denotes a 1T-2H $MoS_2$ mixed cluster. The calculated spectra for models **A** and **B** resemble the experimental data of 2H-$MoS_2$ and 1T@2H-$MoS_2$, respectively. It then provides support for the formation of 1T-$MoS_2$ in the 2H-$MoS_2$ nanosheets, in agreement with the HRTEM results. The XPS measurements also indicate that upon doping 1T-$MoS_2$, peaks at around 229 and 232 eV that correspond to binding energies of $Mo^{4+}$ $3d_{5/2}$ and $3d_{3/2}$ electrons in 2H-$MoS_2$ are shifted to lower energy side by 0.5 eV (Figure 3b), a phenomenon also observed by Eda et al. for 1T-$MoS_2$.[34] The deconvolution of Mo and S XPS peaks further reveals additional peaks at the lower energy along with the initial peaks of 2H-$MoS_2$, and the relative content of 1T phase is estimated to be ~25% according to the literature reports.[35]


DOI: 10.1021/ja5120908
J. Am. Chem. Soc. 2015, 137, 2622–2627

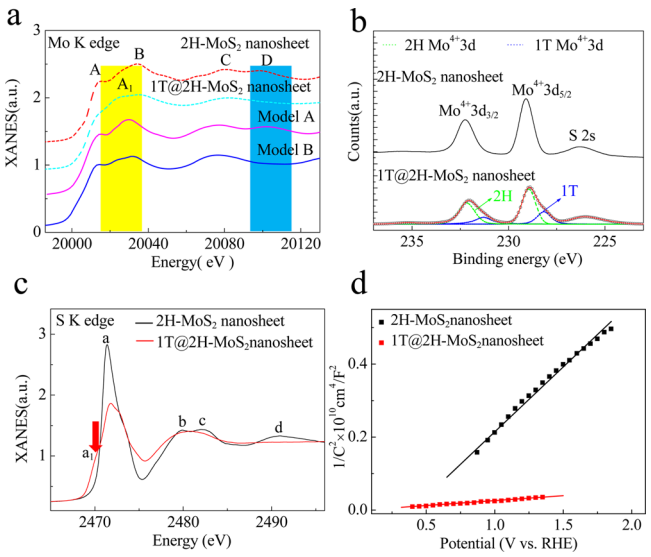


**Figure 3.** (a) Experimental Mo K-edge XANES spectra of the 2H-$MoS_2$ and 1T@2H-$MoS_2$ nanosheets, together with the calculated spectra for two model structures: 2H-$MoS_2$ cluster (model **A**) and 1T-2H $MoS_2$ mixed cluster (model **B**). (b) XPS spectra of the 2H-$MoS_2$ and 1T@2H-$MoS_2$ nanosheets. The blue and green dotted curves represent the contributions of 1T and 2H phases to the Mo 4d peaks in the 1T@2H-$MoS_2$ nanosheets, respectively. (c) S K-edge XANES spectra, and (d) Mott–Schottky plot of the 2H-$MoS_2$ and 1T@2H-$MoS_2$ nanosheets.

This concentration is consistent with the results determined from HRTEM images and XANES spectra (see some details in the Supporting Information). XPS and ICP results (Table S1) clearly exhibit that the Mo:S molar ratio is significantly decreased from about 1:1.99 to 1:1.90 after incorporating the 1T-$MoS_2$ phase into the 2H-$MoS_2$ matrix, consistent with the existence of a substantial number of S vacancies.

Sulfur K-edge XANES spectra (Figure 3c) were also used to understand how the incorporated 1T-$MoS_2$ influences the 2H-$MoS_2$ nanosheets. Like bulk 2H-$MoS_2$, the 2H-$MoS_2$ nanosheets also show four characteristic XANES peaks of a (~2471 eV), b (~2479 eV), c (~2482 eV), and d (~2491 eV).[36] Peak a is known to arise from the electron transition of S 1s electrons to unoccupied hybridized orbitals of S 3p and Mo 4d, and peaks b and c correspond to the transition to p-like final states.[37] Compared with the 2H-$MoS_2$ nanosheets, the 1T@2H-$MoS_2$ nanosheets have a lower amplitude of peak a, their peaks b and c are merged, and peak d disappears. More strikingly, there appears a shoulder peak $a_1$ at the position (~2470 eV) just below peak a, implying the existence of a new energy level near the Fermi level of 2H-$MoS_2$. Correspondingly, the Mo $L_3$-edge XANES spectra in Figure S5 also indicate considerably widened energy states distribution related to Mo 4d electrons after incorporating the 1T-$MoS_2$ phase, with the appearance of some unoccupied Mo 4d states (as labeled by an arrow). These observations suggest a noticeable change of the band structure of 2H-$MoS_2$ caused by 1T phase, i.e., a new bandgap energy state with Mo 4d character is produced. Generally, for a semiconductor with dopant ion concentration higher than $10^{18}/cm^3$, the dopant states can be hybridized to a dopant band.[38] In the 1T@2H-$MoS_2$ nanosheets, the relative content of 1T phase is ~25% and the introduced $t_{2g}$ band gap states is delocalized. Thus, it could be expected that the intrinsic electrical property of 2H-$MoS_2$ semiconductor has been changed by the 1T-$MoS_2$ phase. To confirm this point, the Mott–Schottky method is further used to determine the carrier density of the samples, and the results are shown in Figure 3d. It is clearly displayed that both nanosheet samples are n-type semiconductor. The determination of curve slope reveals that the electron concentration of 1T@2H-$MoS_2$ nanosheets is about 10 times larger than that of the 2H-$MoS_2$ nanosheets, most possibly due to the presence of the delocalized Mo 4d-like bandgap energy states.

For an in-depth understanding on how the room-temperature ferromagnetism of 2H-$MoS_2$ nanosheets is induced by the Mo ions with nonzero magnetic moments, the electronic structure calculations were performed. The calculation details are included in the Supporting Information. Considering the four-layer thickness of the 2H-$MoS_2$ nanosheets, we built three structural models of 2H-$MoS_2$ with four-layer thickness containing embedded 1T and/or sulfur vacancy: perfect 2H-$MoS_2$, 1T-$MoS_2$, and 1T- incorporated 2H-$MoS_2$. The obtained density of states (DOS) are displayed in Figure 4a. First of all,

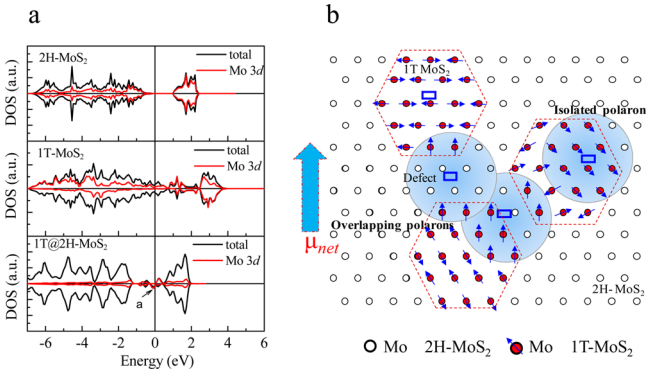


**Figure 4.** (a) Calculated DOS for various model structures: 2H-$MoS_2$, 1T-$MoS_2$, and 1T@2H-$MoS_2$ nanosheets. (b) Representation of magnetic polarons.

calculations of the formation energy indicate that the presence of $V_S$ is favorable for the transition from trigonal prismatic to octahedral coordination of Mo ions in 2H-$MoS_2$, due to the extra electrons induced by $V_S$ (Figure S6). The impact of extra electrons on the 2H-to-1T transition of Mo coordination has also been reported by Wang et al. for Li-doped 2H-$MoS_2$.[25] Besides, the phase transition is promoted by the 2D structure of nanosheets, because the quantum-confinement effect raises the energy of empty Mo 4d states and reduces the stability of 2H-$MoS_2$.[15,39,40] Seen from the calculated DOS results (Figure 4a), the four-layer-thick 2H-$MoS_2$ exhibits the semiconductor characteristics, with the conduction and valence bands composed mainly of Mo 4d orbitals. By contrast, the 1T-$MoS_2$ layer displays metallic character, as indicated by the noticeable Mo 4d states across the Fermi energy. In the framework of crystal field theory,[26] the semiconducting nature of 2H-$MoS_2$ stems from the symmetry-induced splitting of the Mo 4d orbitals of a $D_{3h}$-$MoS_6$ unit into three groups: (1) completely occupied Mo $4d_{z^2}$, (2) Mo $4d_{xy}$, and Mo $4d_{x^2-y^2}$, and (3) unoccupied Mo $4d_{xz}$ and Mo $4d_{yz}$ (Figure S7). The metallic character of 1T-$MoS_2$ comes from the fact that the Mo 4d orbitals under the coordination of octahedral ligand are split into triple-degenerate $t_{2g}$ ($d_{xy}$, $d_{xz}$, $d_{yz}$) and double-degenerate $e_g$ sets, with the $t_{2g}$ orbitals partly occupied by the two 4d electrons (Figure S7). In spite of the atomic moment of 2 $\mu_B$ per $Mo^{4+}$ in 1T-$MoS_2$, the magnetic energy ($\Delta E = E_{FM} - E_{AFM}$)


DOI: 10.1021/ja5120908
J. Am. Chem. Soc. 2015, 137, 2622–2627

calculations show that the electron spin exchange interactions between $Mo^{4+}$ ions are still antiferromagnetic in the 1T phase. Therefore, the 1T phase alone is not able to lead to significant ferromagnetism at room temperature. When the 1T phase is incorporated into 2H-$MoS_2$, a bandgap energy state *a* with $Mo^{4+}$ 4d feature is observed, consistent with the XANES results (Figure 3c). This is presumably caused by electronic interactions between $Mo^{4+}$ ions in the 1T and 2H phases.

Finally, we discuss briefly the physical origin of the observed ferromagnetism of the 2H-$MoS_2$ and 1T@2H-$MoS_2$ nanosheets. Bulk 2H-$MoS_2$ is known to be macroscopically nonmagnetic, because the $Mo^{4+}$ ions are in a trigonal prismatic local coordination, in which the two 4d electrons are spin-antiparallel and the net magnetic moment is zero (Figure S7). For 2H-$MoS_2$ nanosheets, the weak ferromagnetism mainly comes from the complex consisting of S vacancy, and the $Mo^{4+}$ ions do not contribute to the magnetic moments. In 1T@2H-$MoS_2$ nanosheets which exhibit robust ferromagnetism, the increased carrier density could not explain their enhanced magnetism and the bound magnetic polaron (BMP) model is more suitable to explain the magnetic origin.[41] According to the average size (2 nm) and concentration (~25%) of the 1T-$MoS_2$ phase in 1T@2H-$MoS_2$ nanosheets, the distances between two neighboring 1T-$MoS_2$ regions have the highest distribution probability at 1−3 nm (see Figure S8 and the details in the Supporting Information), smaller than the size of a polaron which is generally <3 nm.[41] Then the spins of the localized defects (S vacancy) align those of the nearby Mo ions in the 1T phase which provide the magnetic moments, producing an effective magnetic field and activating the ferromagnetic interactions between Mo ions within the polaron radius (Figure 4b). It should be addressed that the 1T phase incorporated in the 2H-$MoS_2$ host could not be simply regarded as a secondary phase as commonly observed in diluted magnetic semiconductors. This is because the embedded 1T-$MoS_2$ phase alone could not cause the robust ferromagnetism, but provides a magnetic moment. Only those $Mo^{4+}$ ions located within the effective radius of a same polaron (around a sulfur vacancy center) could interact with each other in a ferromagnetic manner and give rise to the observed ferromagnetism of the 1T@2H-$MoS_2$ nanosheets.

## CONCLUSIONS

In summary, we have experimentally demonstrated the feasibility of achieving ferromagnetic interactions in a typical transition-metal dichalcogenide $MoS_2$ nanosheet, by incorporating 1T phase of $MoS_2$ into 2H-$MoS_2$ nanosheet host. As shown by a detailed study of structural and magnetic properties, this strategy could lead to a Curie temperature of 395 K and enhance greatly the saturation magnetization of 2H-$MoS_2$ nanosheets at 300 K from 0.02 to 0.25 $\mu_B$/Mo. Based on the EPR experiment and first-principles calculations, we propose that the observed robust ferromagnetism of 1T-$MoS_2$ incorporated 2H-$MoS_2$ nanosheets originates from the exchange interactions between sulfur vacancies and $Mo^{4+}$ ions. It is worthy to note that such a strategy does not change the overall distributions of Mo ions in the 2H phase. This idea is expected to be generalized to tune the magnetic properties of other two-dimensional materials.

## EXPERIMENTAL SECTION

**Synthesis of $MoS_2$ Ultrathin Nanosheets.** Typically, 1 mmol $(NH_4)_6Mo_7O_{24}\cdot 4H_2O$ and 30 mmol thiourea were dissolved in 40 mL distilled water under vigorous stirring to form a homogeneous solution. After being stirred for 1 h, the solution was transferred into a 50 mL Teflon-lined stainless steel autoclave and maintained at 200 °C for 20 h. Then the reaction system was allowed to cool down to room temperature naturally. The obtained products were collected by centrifugation and washed with ethanol. Then the stoichiometric $MoS_2$ nanosheets were subjected to centrifugation and ultrasonation in ethanol solution and once more autoclavation under 220 °C for 8 h to form the final products and dried at 60 °C under vacuum.

**Structure and Property Characterization.** XRD patterns were recorded by using a Philips X'Pert Pro Super diffractometer with Cu K$\alpha$ radiation ($\lambda$ = 1.54178 Å). The transmission electron microscopy (TEM) was carried out on a JEM-2100F field emission electron microscope at an acceleration voltage of 200 kV. The high-resolution TEM (HRTEM), and corresponding energy-dispersive spectroscopy (EDS) mapping analyses were performed on a JEOL JEM-ARF200F TEM/STEM with a spherical aberration corrector. Atomic force microscopy (AFM) study in the present work was performed by means of Veeco DI Nanoscope MultiMode V system. X-ray photoelectron spectra (XPS) were acquired on an ESCALAB MKII with Mg K$\alpha$ ($h\nu$ = 1253.6 eV) as the excitation source. The binding energies obtained in the XPS spectral analysis were corrected for specimen charging by referencing C 1s to 284.5 eV. S and Mo concentrations were determined by inductively coupled plasma atomic emission spectrometry (ICP-AES, Jarrel Ash model 955). Magnetization studies were carried out using a superconducting quantum interference device (SQUID) magnetometer ($T$ < 300 K). High-temperature magnetization ($T$ > 300 K) was recorded using a vibrating sample magnetometer (VSM). The Mo $L_3$-edge and S K-edge X-ray absorption near-edge (XANES) spectra were measured at the 4W7B beamline of the Beijing Synchrotron Radiation Facility (BSRF), China, in the total electron yield (TEY) mode by collecting sample drain current under a vacuum better than $5 \times 10^{-8}$ Pa. The beam from a bending magnet was monochromatized with a varied line-spacing plane grating and refocused by a toroidal mirror. The Mo K-edge XAFS spectra were measured at the BL14W1 beamline of the Shanghai Synchrotron Radiation Facility (SSRF), China. The storage ring of BSRF was operated at 2.5 GeV with a maximum current of 250 mA. Electronic paramagnetic resonance (EPR) measurements were performed in a JSE-FA200 EPR spectrometer at X-band (~9 GHz) with a resolution of 2.35 $\mu$T at room temperatures.

## ASSOCIATED CONTENT

### Supporting Information

XRD pattern, EPR spectra, mapping and energy dispersive spectroscopy spectra, XANES calculation, and DFT calculation details and analysis. This material is available free of charge via the Internet at http://pubs.acs.org.

## AUTHOR INFORMATION


### Corresponding Authors

*ywsh2000@ustc.edu.cn
*zhsun@ustc.edu.cn
*sqwei@ustc.edu.cn

### Author Contributions

[§]These authors contributed equally.


### Notes

The authors declare no competing financial interest.

## ACKNOWLEDGMENTS

This work was supported by the National Natural Science Foundation of China (grant nos. 11135008, 11435012, U1332131, U1332111, 11475176, and U1232129), the National Basic Research Program of China (2012CB825804), and the Foundation for Innovative Research Groups of the National Natural Science Foundation of China (11321503). The authors



DOI: 10.1021/ja5120908
J. Am. Chem. Soc. 2015, 137, 2622−2627

would like to thank BSRF and SSRF for the synchrotron radiation beamtime.

## REFERENCES

(1) Bianco, E.; Butler, S.; Jiang, S. S.; Restrepo, O. D.; Windl, W.; Goldberger, J. E. *ACS Nano* **2013**, *7*, 4414.
(2) Ganatra, R.; Zhang, Q. *ACS Nano* **2014**, *8*, 4074.
(3) Coleman, J. N.; Lotya, M.; O'Neill, A.; Bergin, S. D.; King, P. J.; Khan, U.; Young, K.; Gaucher, A.; De, S.; Smith, R. J.; Shvets, I. V.; Arora, S. K.; Stanton, G.; Kim, H. Y.; Lee, K.; Kim, G. T.; Duesberg, G. S.; Hallam, T.; Boland, J. J.; Wang, J. J.; Donegan, J. F.; Grunlan, J. C.; Moriarty, G.; Shmeliov, A.; Nicholls, R. J.; Perkins, J. M.; Grieveson, E. M.; Theuwissen, K.; McComb, D. W.; Nellist, P. D.; Nicolosi, V. *Science* **2011**, *331*, 568.
(4) Nicolosi, V.; Chhowalla, M.; Kanatzidis, M. G.; Strano, M. S.; Coleman, J. N. *Science* **2013**, *340*, 1420.
(5) Wang, Q. H.; Kalantar-Zadeh, K.; Kis, A.; Coleman, J. N.; Strano, M. S. *Nat. Nanotechnol.* **2012**, *7*, 699.
(6) Chhowalla, M.; Shin, H. S.; Eda, G.; Li, L. J.; Loh, K. P.; Zhang, H. *Nat. Chem.* **2013**, *5*, 263.
(7) Sangwan, V. K.; Arnold, H. N.; Jariwala, D.; Marks, T. J.; Lauhon, L. J.; Hersam, M. C. *Nano Lett.* **2013**, *13*, 4351.
(8) Radisavljevic, B.; Radenovic, A.; Brivio, J.; Giacometti, V.; Kis, A. *Nat. Nanotechnol.* **2011**, *6*, 147.
(9) Radisavljevic, B.; Whitwick, M. B.; Kis, A. *ACS Nano* **2011**, *5*, 9934.
(10) Zhu, Z. Y.; Cheng, Y. C.; Schwingenschlogl, U. *Phys. Rev. B* **2011**, *84*, 153402.
(11) Guo, Y.; Dai, J.; Zhao, J.; Wu, C.; Li, D.; Zhang, L.; Ning, W.; Tian, M.; Zeng, X. C.; Xie, Y. *Phys. Rev. Lett.* **2014**, *113*, 157202.
(12) Han, S. W.; Hwang, Y. H.; Kim, S.-H.; Yun, W. S.; Lee, J.; Park, M. G.; Ryu, S.; Park, J. S.; Yoo, D.-H.; Yoon, S.-P. *Phys. Rev. Lett.* **2013**, *110*, 247201.
(13) Yan, W.; Liu, Q.; Wang, C.; Yang, X.; Yao, T.; He, J.; Sun, Z.; Pan, Z.; Hu, F.; Wu, Z.; Xie, Z.; Wei, S. *J. Am. Chem. Soc.* **2014**, *136*, 1150.
(14) Dalpian, G. M.; Chelikowsky, J. R. *Phys. Rev. Lett.* **2006**, *96*, 226802.
(15) Komsa, H. P.; Kotakoski, J.; Kurasch, S.; Lehtinen, O.; Kaiser, U.; Krasheninnikov, A. V. *Phys. Rev. Lett.* **2012**, *109*, 035503.
(16) Zheng, H. L.; Yang, B. S.; Wang, D. D.; Han, R. L.; Du, X. B.; Yan, Y. *Appl. Phys. Lett.* **2014**, *104*, 132403.
(17) Zhang, Z.; Zou, X.; Crespi, V. H.; Yakobson, B. I. *ACS Nano* **2013**, *7*, 10475.
(18) Zou, X.; Liu, Y.; Yakobson, B. I. *Nano Lett.* **2012**, *13*, 253.
(19) Joswig, J.-O.; Lorenz, T.; Seifert, G. *ACS Nano* **2013**, *7*, 10449.
(20) Zhang, J.; Soon, J. M.; Loh, K. P.; Yin, J.; Ding, J.; Sullivian, M. B.; Wu, P. *Nano Lett.* **2007**, *7*, 2370.
(21) Gao, D.; Si, M.; Li, J.; Zhang, J.; Zhang, Z.; Yang, Z.; Xue, D. *Nanoscale Res. Lett.* **2013**, *8*, 1.
(22) Zhang, Z. H.; Zou, X. L.; Crespi, V. H.; Yakobson, B. I. *ACS Nano* **2013**, *7*, 10475.
(23) Kan, M.; Wang, J. Y.; Li, X. W.; Zhang, S. H.; Li, Y. W.; Kawazoe, Y.; Sun, Q.; Jena, P. *J. Phys. Chem. C* **2014**, *118*, 1515.
(24) Lin, Y. C.; Dumcencon, D. O.; Huang, Y. S.; Suenaga, K. *Nat. Nanotechnol.* **2014**, *9*, 391.
(25) Wang, L. F.; Xu, Z.; Wang, W. L.; Bai, X. D. *J. Am. Chem. Soc.* **2014**, *136*, 6693.
(26) Enyashin, A. N.; Yadgarov, L.; Houben, L.; Popov, I.; Weidenbach, M.; Tenne, R.; Bar-Sadan, M.; Seifert, G. *J. Phys. Chem. C* **2011**, *115*, 24586.
(27) Sun, Y. H.; Liu, K.; Hong, X. P.; Chen, M.; Kim, J.; Shi, S. F.; Wu, J. Q.; Zettl, A.; Wang, F. *Nano Lett.* **2014**, *14*, 5329.
(28) Ding, Q.; Meng, F.; English, C. R.; Caban-Acevedo, M.; Shearer, M. J.; Liang, D.; Daniel, A. S.; Hamers, R. J.; Jin, S. *J. Am. Chem. Soc.* **2014**, *136*, 8504.
(29) Lukowski, M. A.; Daniel, A. S.; Meng, F.; Forticaux, A.; Li, L.; Jin, S. *J. Am. Chem. Soc.* **2013**, *135*, 10274.
(30) Arizumi, T.; Mizutani, T.; Shimakaw, K. *Jpn. J. Appl. Phys.* **1969**, *8*, 1411.
(31) Blinc, R.; Cevc, P.; Mrzel, A.; Arcon, D.; Remskar, M.; Milia, F.; Laguta, V. V. *Phys. Status Solidi B* **2010**, *247*, 3033.
(32) Ochsenbein, S. T.; Feng, Y.; Whitaker, K. M.; Badaeva, E.; Liu, W. K.; Li, X. S.; Gamelin, D. R. *Nat. Nanotechnol.* **2009**, *4*, 681.
(33) Ataca, C.; Ciraci, S. *J. Phys. Chem. C* **2011**, *115*, 13303.
(34) Eda, G.; Yamaguchi, H.; Voiry, D.; Fujita, T.; Chen, M. W.; Chhowalla, M. *Nano Lett.* **2011**, *11*, 5111.
(35) Eda, G.; Fujita, T.; Yamaguchi, H.; Voiry, D.; Chen, M.; Chhowalla, M. *ACS Nano* **2012**, *6*, 7311.
(36) Guay, D.; Divigalpitiya, W. M. R.; Belanger, D.; Feng, X. H. *Chem. Mater.* **1994**, *6*, 614.
(37) Li, D.; Bancroft, G. M.; Kasrai, M.; Fleet, M. E.; Feng, X. H.; Tan, K. H. *Phys. Chem. Miner.* **1995**, *22*, 123.
(38) Peng, Y.; He, J.; Liu, Q.; Sun, Z.; Yan, W.; Pan, Z.; Wu, Y.; Liang, S.; Cheng, W.; Wei, S. *J. Phys. Chem. C* **2011**, *115*, 8184.
(39) Py, M. A.; Haering, R. R. *Can. J. Phys.* **1983**, *61*, 76.
(40) Donarelli, M.; Bisti, F.; Perrozzi, F.; Ottaviano, L. *Chem. Phys. Lett.* **2013**, *588*, 198.
(41) Coey, J. M. D.; Venkatesan, M.; Fitzgerald, C. B. *Nat. Mater.* **2005**, *4*, 173.



DOI: 10.1021/ja5120908
*J. Am. Chem. Soc.* 2015, 137, 2622−2627